(Proposal to Jefferson Lab PAC 40)

Neutral Particle Spectrometer Facility in Hall C

May 5, 2013

A. Camsonne, R. Ent, P. Nadel-Turoński, S.A. Wood, B. Wojtsekhowski
Jefferson Lab, Newport News, VA 23606

A. Asaturyan, A. Mkrtchyan, H. Mkrtchyan, V. Tadevosyan,
S. Zhamkochyan
A.I. Alikhanyan National Science Laboratory, Yerevan 0036, Armenia

M. Guidal, C. Munoz Camacho, R. Paremuzyan
Institut de Physique Nucleaire d'Orsay, IN2P3, BP 1, 91406 Orsay, France

I. Albayrak, M. Carmignotto, J. Dénes-Couto, N. Hlavin, T. Horn[1]
F. Klein, B. Nepal
The Catholic University of America, Washington, DC 20064

C. Hyde, M.N.H. Rashad
Old Dominion University, Norfolk, Virginia

P. King, J. Roche
Ohio University, Athens, OH 45701

D. Day, D. Keller, O. Rondon
University of Virginia, Charlottesville, VA, USA

D. Hamilton
University of Glasgow, Glasgow, Scotland, UK

S. Sirca
University of Ljubljana, Ljubljana, Slovenia

[1] Contact person: hornt@jlab.org

Contents

I. INTRODUCTION

We plan to augment the capability of Hall C for precision cross section measurements of charged particles with a general-purpose and remotely rotatable neutral particle spectrometer (NPS). The proposed neutral particle detection system can be used in conjunction with Hall C's well-understood High-Momentum Spectrometer (HMS) for high-precision absolute cross section measurements at Jefferson Lab within the 12-GeV era [1] . It also facilitates from the wide range accessible with HMS, with an angle range between 10.5° and ∼80°, and a central momentum reach of up to 7.3 GeV/c. In coincidence, systematic point-to-point uncertainties of well below 2% are foreseen with this setup.

This neutral particle detection system is cantelevered of, or positioned on, the SHMS carriage to allow for two flexible remote-rotatable angle ranges from 5.5°-30°, and from 20°-60°, and consists of the following elements: i) a sweeping magnet; ii) a 25 msr $PbWO_4$-based neutral particle detector; iii) high voltage distribution bases with built-in amplifiers for operation in high-rate environments; iv) essentially deadtime-less digitizing electronics; v) a dedicated beam pipe to reduce backgrounds.

The facility will allow precision measurements requiring photon or neutral-pion detection in coincidence with the existing and well-understood Hall C High-Momentum Spectrometer to detect the scattered electrons (or recoiling protons). It can be used as photon detector for Deeply-Virtual Compton Scattering or Wide-Angle Compton Scattering reactions benefitting from the accessible range of HMS. It can also be used as neutral-pion detector, where the neutral pion will be detected by measurement of its $\gamma\gamma$ decay products in a dedicated neutral-pion detector.

To reduce electromagnetic backgrounds, we plan to use a conventional sweeping magnet, similar but with only ∼10% of the field requirements as the Horizontal-Bend magnet presently under construction for the new Hall C/SHMS to maintain access to small-angle (∼ 5.5°) π° detection. Detailed background simulations show this setup safely allows for 2 μA beam current on a 10 cm long cryogenic LH2 target down to the very smallest NPS angles, and much higher luminosities at more backward angles.

II. EXPERIMENTAL SETUP

We propose to make a precision coincidence setup measuring charged particles (scattered electrons or recoiling protons) with the existing HMS and photons, either single photons or from the decay of neutral pions, in a neutral particle channel using a $PbWO_4$ calorimeter. A high luminosity spectrometer+calorimeter system like the HMS+$PbWO_4$ combination in Hall C is well suited for such measurements. The magnetic spectrometers benefit from relatively small point-to-point uncertainties, which are crucial for absolute cross section measurements such as those needed for meaningful L-T separations. In particular, the optics properties and the acceptance of the HMS have been studied extensively and are well understood in the kinematic range between 0.5 and 5 GeV, as evidenced by more than 200 L/T separations (∼ 1000 kinematics) [2]. The position of the elastic peak has been shown to be stable to better than 1 MeV, and the precision rail system and rigid pivot connection have provided reproducible spectrometer pointing for about a decade.

A. NPS Facility Overview

We will construct a general-purpose and remotely rotatable NPS system for Hall C. A floor layout of the HMS and the proposed NPS system is shown in Fig. 1(a). This system consists of the following elements:

- A sweeping magnet providing 0.3 Tm field strength, with similar outer geometry as the Horizontal-Bend (HB) Magnet presently under construction for the SHMS but with conventional copper coils.
- A neutral particle detector consisting of 1116 $PbWO_4$ blocks (similar to the PRIMEX [3] experimental setup, see Fig. 1(b)) in a temperature controlled frame, comprising a 25 msr device at a distance of 4 meters.

- Essentially deadtime-less digitizing electronics to independently sample the entire pulse form for each crystal allowing for background subtraction and identification of pile-up in each signal. This is a major improvement over the existing PRIMEX apparatus.

- A new set of high voltage distribution bases with built-in amplifiers for operation in high-rate environments.

- Cantelevered platforms of the SHMS carriage, to allow for precise and remote rotation around the Hall C pivot of the full Neutral Particle Spectrometer, over an angle range between 5.5 and 30 degrees.

- A dedicated beam pipe with as large critical angle as possible to reduce backgrounds beyond the HB-type sweeping magnet.

To provide space for this sweeping magnet, the HB magnet for the SHMS needs to be removed. The HB adds a 3 degree horizontal pre-bend to the SHMS to allow reaching the smallest angles, as compared to an 18 degree vertical bend. Thus, it only provides a small perturbation to the SHMS optics, and as such removing and reinstalling the HB magnet does not impact the final SHMS optics understanding, given proper attention to alignment. In fact, the SHMS is in this sense comparable to the earlier SOS optics, where removing and properly reinstalling and realigning the SOS quadrupole did not imply additional optics understanding work beyond the standard sieve-slit calibration runs.

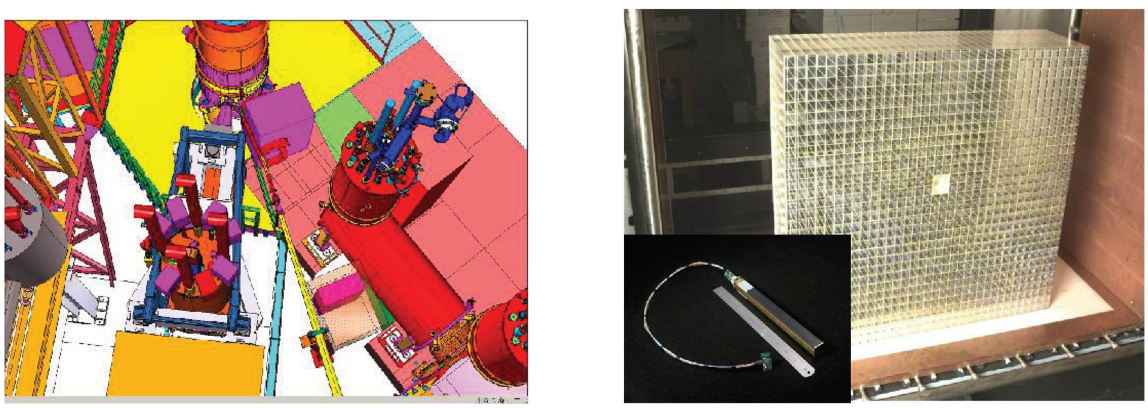

(a) (b)

FIG. 1: *(a)The NPS detector in Hall C. The cylinder at the top center is the (1 m diameter) vacuum chamber containing the 10 cm long liquid-hydrogen target. The long yellow tube emanating from the scattering chamber on the lower right is the downstream beam pipe. To the left of the beam pipe is the HMS. Only the liquid He and liquid N_2 lines for the large superconducting quadrupoles at the entrance to the spectrometer are clearly visible. To the right of the beam line, the first quadrupole of the SHMS and its cryogenic feed lines are shown. This spectrometer will be used for π° experiments as a carriage to support the $PbWO_4$ calorimeter (shown in its light-tight and temperature control box next to the beam line) and the associated sweep magnet. (b) The high resolution $PbWO_4$ part of the HYCAL [4] on which the present design is based.*

The sweeping magnet will be a conventional version of the HB magnet presently under construction, with copper coils to effectively use the full bore of such a magnet (35 by 36 cm^2). In sharp contrast to the superconducting HB magnet, which provides a field strength of 1.93 Tm, we only require a 0.3 Tm field to sweep away charged particles up to 300 MeV/c. This modest field requirement is well within the range of conventional magnet coils, alleviating the need for additional cryogenic and inner vacuum cans. The sweeping magnet design is matched to existing JLab power supplies and existing commercial conductors. The materials for the coil, a 24 m of copper conductor of dimension 0.5x0.5 in^2, including a 1/4 inch diameter water cooling channel, could be obtained from, for instance, Luvata-Finnland. The coil winding tools could be obtained through AES-Penn. The materials for the yoke steel could be obtained from vendors like Oakland Steel and would be purchased in slabs of 4" for easier machining in university machine shops. These magnet component vendors also supplied the respective components for the Hall A PREX magnet. The estimated radiation dose at the location of the magnet (< 30,000 rem/hr) was folded into decisions for radiation hard resins and insulation systems.

The obvious advantage of using a sweeping magnet cloning the geometric properties of the HB magnet is that it has a relatively large bore, of 35 by 36 cm^2, and is designed from the start to reach small scattering angles without impacting the main electron beam. The effective gap for an HB-type magnet for neutral particle may be slightly reduced, as the coil assumes a 3 degree horizontal pre-bend for charged particles. Thus, if we assume a direct clone of the HB the effective gap for neutral particles (assuming symmetric acceptance around the detection angle) is reduced to about 30 by 36 cm^2. This problem likely gets alleviated for a conventional magnet but we have assumed the latter aperture for the rate estimates. We found that we can move the "HB-clone" sweeping magnet about 20 cm forwards as compared to the HB, such that the magnetic center is at a distance of 1.57 m from the pivot. This then constitutes a solid angle of 25.5 msr, with $\sim$146 mrad horizontal and $\sim$175 mrad vertical acceptance (taking into account a vacuum can of 1 meter length).

B. $PbWO_4$ Detector

Projecting this to a distance of 4 meters, the front face of the $PbWO_4$ calorimeter, implies a detector of 58 cm wide and 70 cm high. This corresponds to 29 by 34 $PbWO_4$ crystals of 2.05 by 2.05 cm^2 (each 18.0 cm long). We have added one crystal on each side to properly capture showers, and thus designed our $PbWO_4$ calorimeter to consist of 31 by 36 $PbWO_4$ crystals, or 64 by 74 cm^2. This amounts to a requirement of 1116 $PbWO_4$ crystals, less than the 1152 used in the Hybrid Calorimeter of the PRIMEX experiment.

To reject very low-energy background, a thin absorber could be installed in front of the $PbWO_4$ detector. Other experiments may add a veto detector in front of the crystals, for instance consisting of 5 mm-thick segmented scintillator counters, to reject high-energy charged particles that are not deflected by the sweeper magnet. The space between the sweeper magnet and the proximity of the $PbWO_4$ detector will be enclosed within a vacuum channel (with a thin exit window, further reducing low-energy background) to minimize the decay photon conversion in air.

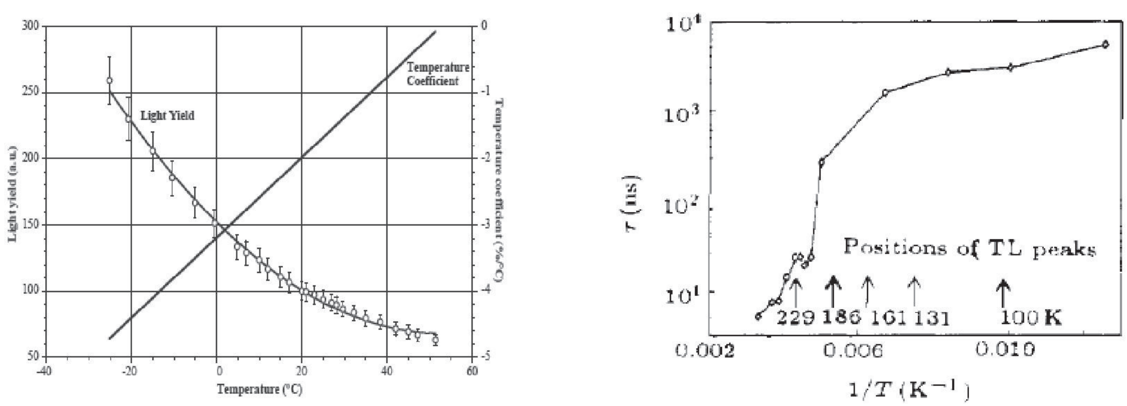

(a) (b)

FIG. 2: *Temperature dependences of the light yield (a) and the decay time of the emission of the λ=400 nm light (b) for the crystal $PbWO_4$. Figure (a) is adopted from P. Lecoq et al. [5], and (b) from Shi Chao-Shu, Chin [6].*

The emission of $PbWO_4$ includes up to three components, and decay time increases with wave length: τ_1 $\sim$5 ns (73%); τ_2 $\sim$14 ns (23%) for emission of λ in the range of 400-550 nm; τ_3 has lifetime more than 100 ns, but it counts only $\sim$4% of the total intensity. The light yield and the decay time of the $PbWO_4$ are temperature dependent, with the light yield increasing at low temperature (Fig. 2(a)), but the decay time (drastically) decreasing at room temperature, as illustrated shown in Fig. 2(b).

Given the temperature sensitivity of the scintillation light output of the $PbWO_4$ crystals, the entire calorimeter must be kept at a constant temperature, to within 0.1° to guarantee 0.5% energy stability for absolute calibration and resolution. The high-voltage dividers on the PMTs may dissipate up to several hundred Watts, and this power similarly must not create temperature gradients or instabilities in the calorimeter. The π^0 calorimeter will thus be thermally isolated and be surrounded on all four sides by water cooled copper plates. This design is based on that of the HYCAL temperature controlled frame and optimized with more recent experience from CMS [7], which has shown stability to 0.05° C. The materials for the frame are foreseen to include steel and steel alloy plates, copper plates, and a temperature control system, and the design accomodates a geometrical arrangement in an array of 36 by 31 crystals.

At the anticipated background rates (see section III B), pile-up and the associated baseline shifts can adversely affect the calorimeter resolution, thereby constituting the limiting factor for the beam current. The solution is to read out a sampled signal, and perform offline shape analysis using a flash ADC (fADC) system (see section II B 2). New HV distribution bases with built-in pre-amplifiers (see section III D) will allow for operating the PMTs at lower voltage and lower anode currents, and thus protect the photocathodes or dynodes from damage.

The $PbWO_4$ detector for π° detection is located at a distance of 4 meters, and the dimensions of the $PbWO_4$ crystals are 2.05 x 2.05 cm^2. The typical position resolution is 2-3 mm. Each crystal covers 5 mrad, and the expected angular resolution is 0.5-0.75 mrad, which is comparable with the resolutions of the HMS and SOS, routinely used for Rosenbluth separations in Hall C. This can also be compared with the CLAS Inner Calorimeter (IC), which has crystals of dimensions 1.33 x 1.33 cm^2 at the front face, located at a distance of 0.8 m from the target. The CLAS IC has reached an angular resolution of 3-4 mrad [8]. Note that compared to the CLAS IC in our case the solid angle per crystal in reduced by a factor of 2.1.

The momentum resolution for exclusively-produced neutral-pions amounts to better than 1%. All these are sufficient given the anticipated less-drastic t-dependence of exclusive ^{1}H(e,e$'\pi^\circ$)p channel as compared to ^{1}H(e,e$'\pi^+$)n.

1. Geometric Acceptance of the Neutral Particle Detector

The $PbWO_4$ neutral pion detection system can in principle measure either one decay photon or two decay photons from the $N(e, e'\pi^\circ)X$ process. We consider here only events with both decay photons detected, as a means to determine the π° electroproduction cross sections. The $\pi^\circ \to \gamma\gamma$ decay is isotropic in the pion rest frame. For exclusive π° production, the electroproduced π° captures the full momentum transfer vector $\vec{q}$, and there is a strong forward boost of the decay toward the calorimeter resulting in good π° acceptance. For neutral pions following a semi-inclusive scattering process, the acceptance will become negligible at small z, where the π° momentum becomes smaller and the $\gamma\gamma$ decay angle larger, preventing coincidence γ detection. In a typical experimental configuration at a 12-GeV Jefferson Lab with a three-momentum transfer of 5.5 GeV/c, this happens at $z \sim 0.3$, where the pion energy is reduced to $E_\pi \sim 1.5$ GeV.

The geometric acceptance of the π° detector was estimated by means of a Monte Carlo calculation. The direction of the primary π° was sampled within the acceptance of the detector, with subsequent π° decay into two γ's. The fraction of events where both γ's were simultaneously detected in the calorimeter was used to calculate the geometric acceptance.

The pions originated from an assumed distance of 4 meters to the calorimeter. A Gaussian distribution of transverse momentum of the π° relative to the direction of the virtual photon was assumed. The virtual photon pointed to the center of the calorimeter, and the slope parameter of the exponential transverse momentum p_T distribution, b=4.661 (GeV/c)$^{-2}$, was assumed (similar to a typical b value found in charged pion production). The prompt pion decay in two photons was sampled uniformly in the π° Center-of-Mass frame, and then the γ's were boosted into the lab frame. Cases with both γ's hitting the active area of the calorimeter and energies of at least 100 MeV were scored.

An example of the geometric acceptance for the chosen detector configuration and a π° momentum in the range from 1.0 to 10 GeV/c is listed in Table I, and shown in Fig. 3. The acceptance rises with pion energy (or

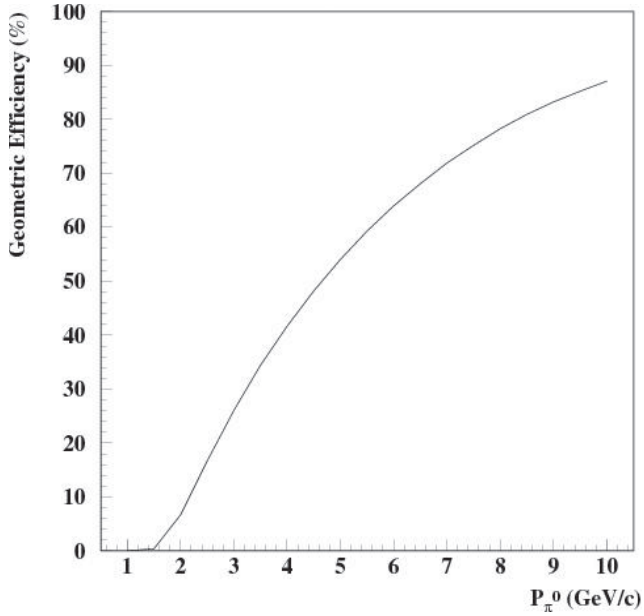

FIG. 3: The geometric acceptance of Neutral Particle Spectrometer as a function of pion momentum P_{π°.

z) due to the decrease in the $\gamma\gamma$ opening angle. Even at the highest energies, the opening angle will still be of the order of 50 mrad, providing ample separation between the two shower centroids of the decay photons, given an expected angular resolution of about 0.7 mrad (or better) for the $PBWO_4$ π° detector.

P_{π° (GeV/c)	1.0	1.5	2.0	2.5	3.0	3.5	4.0	4.5	5.0	5.5	6.0	6.5	7.0	7.5	8.0	8.5	9.0	9.5	10.0
Acceptance (%)	0.0	0.4	6.7	16.7	26.1	34.4	41.7	48.2	54.1	59.2	63.9	68.1	71.9	75.2	78.3	80.9	83.2	85.2	87.1

TABLE I: *Geometric acceptance of π° detection in a calorimeter with an 58 $\times$ 70 cm^2 active area at 4 m distance from target.*

To estimate the efficiency of selecting a photon pair from other processes at forward angles, several background simulations were performed to study the combinatoric background. The distance of the calorimeter, and relative small size of the $PbWO_4$ crystals, are beneficial for reduction of this combinatoric background. It was found that for the worst-case scenario of neutral-pion detector angle of 6 degrees, for a 1 μA beam current, a 10 cm LH2 target, and a 100 ns coincidence time window to capture the two photons, the combinatoric background is only at the few % level, as shown in Figure 4, before application of any other cuts. Thus, we feel confident that we can understand well the efficiency, and especially its stability under these assumptions. Of course, if less detailed understanding is required, one can scale and easily accept higher luminosity numbers.

To elucidate this further, in Figure 5 we present the anticipated pion detection efficiency and combinatoric background as a function of electronics threshold. This is estimated based upon realistic background simulations by P. Degtiarenko for a 10 cm liquid hydrogen target and 1 μA beam current, at the mentioned small angle of 6.3°. The background simulations will be presented in more detail later on.

2. *Electronics for Neutral Particle Spectrometer*

In this section we will describe the plans for the electronics for (e,e$'\gamma$), or more specific (e,e$'\pi^\circ$) reactions. In the latter case, both photons following the decay of neutral pions will be detected in the $PbWO_4$ calorimeter, in coincidence with the scattered electron. However, for many of the anticipated kinematics pursuing moderate

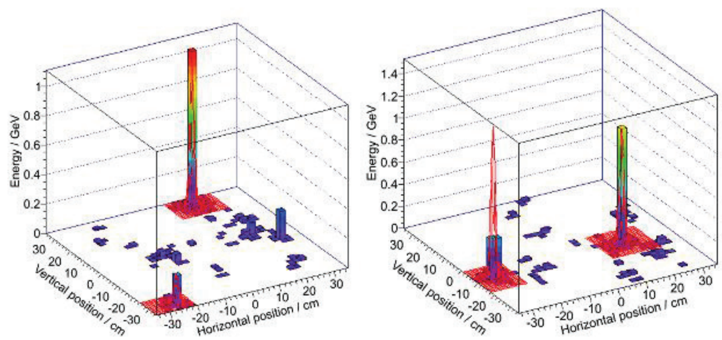

(a) *GEANT4 simulation of photons from π° decay with simulated background of neutral and charged particles, the latter suppressed by the sweeper magnet. The photon pair is selected from other processes in the calorimeter using a cluster finding algorithm.*

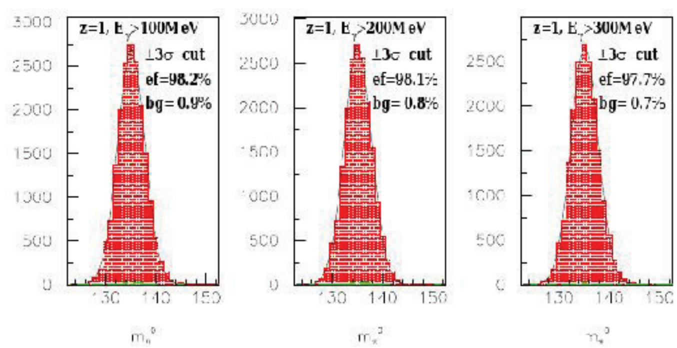

(b) *Reconstructed invariant mass of the π°.*

FIG. 4: Simulations of the $PbWO_4$ calorimeter.

to high four-momentum transfer, the singles rate of electrons in the HMS will be sufficiently low (<1 kHz) to allow using a minimum-bias electron trigger and reading out the π° calorimeter in each event. In this way, exclusive, semi-inclusive, and inclusive cross sections can be compared directly at each kinematic point.

To take full advantage of the high-resolution crystals while operating in a high-background environment, modern flash ADCs (fADCs) will be used to digitize the signal. They continuously sample the signal every 4 ns, storing the information in an internal FPGA memory. When a trigger is received, the samples in a programmable window around the threshold crossing are read out for each crystal that fired. Since the readout of the FPGA does not interfere with the digitizations, the process is essentially deadtime free. If needed, the DAQ system will support windows up to 200-300 ns at 1 kHz and 100% occupancy in the 1200 channel calorimeter ($\sim$ 200 MB/s), but projected data rates will be smaller by orders of magnitude for all presently envisioned kinematics even if the thresholds are set very low. The sampled signals can then be fitted and integrated off-line, effectively eliminating issues with pile-ups, baseline shifts, etc.

For low-Q^2 measurements, where the electron singles rate could be high, the fADC-based system can support a coincidence trigger. Such a trigger would take advantage of the ability of the fADC to perform the integration of the pulse and pass it along to the trigger for cluster finding. The appropriate conditions for the latter can then be used to select, for instance, π° or DVCS events. The integration and cluster finding will delay the trigger decision, but this can be easily accomodated in a pipelined system without any need for delay cables or analog delay modules.

In summary, the system will provide a low dead time, precision signal processing off-line, and support

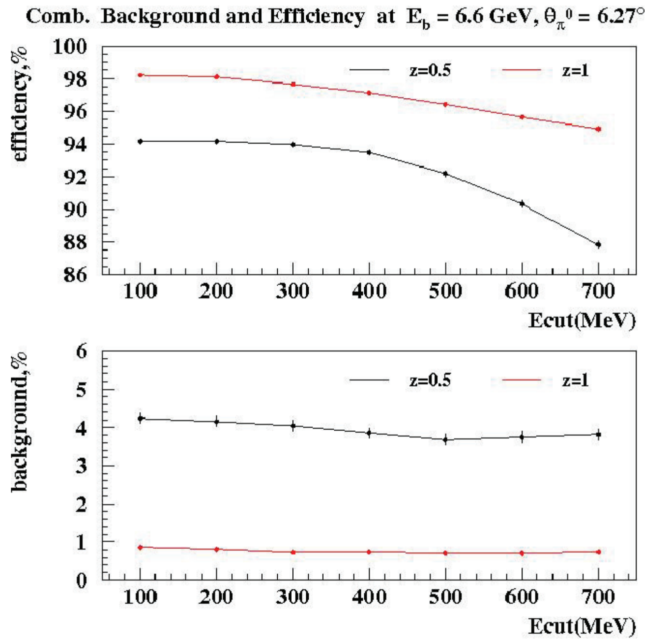

FIG. 5: The pion detection efficiency and combinatoric background as a function of energy threshold.

both high-rate operations in singles mode as well as advanced, trigger-level cluster finding in coincidence mode, As such, it will not only constitute a major advance compared with previous systems used at JLab (*e.g.*, in Hall A), but also make the most effective contribution for improvement of the existing hardware.

C. Setup and Angle Coverage

The major sources contributing to the dose are the target-induced rates themselves, and apertures of the beam line where large-thickness materials such as vacuum flanges are at the closest (critical) distance from the beam. The incident beam will scatter in the target, and (multiple) scattering products will hit such narrow sections first. Subsequently, they will locally deposit almost their full energy in the beam pipe in the form of an electro-magnetic cascade, irradiating a forward angular cone. To minimize this background, a conical or telescopic design of the initial portion of the beam exit line would be useful. This requirement routinely conflicts with the physics need to put the active detectors or spectrometers at forward angles.

Obviously, it is optimal to make the opening or critical angle for the beam exiting the target/scattering chamber region as large as possible.

For instance, if the critical angle would flare out to that determined by the two-feet diameter last section of the beam exit line far downstream, about a degree, then the main cone of scattered electrons would remain inside the vacuum pipe until well beyond the envisioned active detector and its background. This way, the general background in the Hall will be significantly decreased, typically by a few 10's of % at higher beam energies, although much larger at lower beam energies.

The present "standard" critical angle for the Hall C configuration allowing for the smallest spectrometer angles (the so-called "small-angle beam pipe assembly") amounts to an 8.6 mr critical angle, induced by a two-inch diameter beam pipe up to a distance (from the pivot) of 2.96 m. The so-called "large-angle beam pipe" has a two-inch diameter beam pipe to only 1.45 m instead, and thus reaches a critical angle of 17.5 mr, nearly matched to the optimal flare of 1 degrees. However, the HMS can only reach a 15 degree scattering angle with this "large-angle beam pipe" assembly. The reason is that the HMS-Q1 (at a distance of a bit beyond 1.5 m) has a slot on the beam axis side, with a vertical dimension of 2.9 inches.

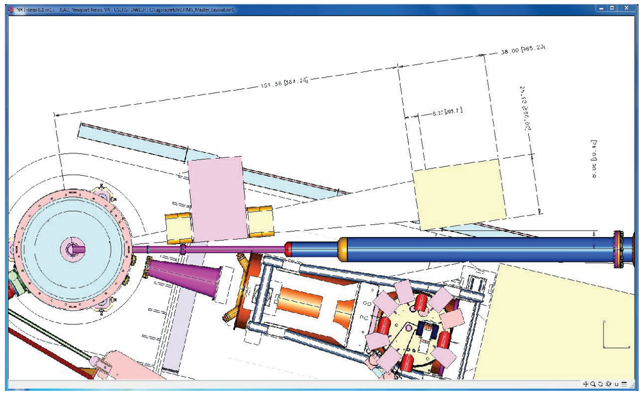

FIG. 6: *Modified beam pipe assembly for the beam dump line. The initial beam pipe has a 2.5 inch diameter up to a distance of 2.35 m, just beyond the area where HMS-Q1 has a slot. Then, the beam pipe has a short section with 6 inch diameter, followed by a long 12-inch diameter section. With this beam pipe, the critical angle will be 13.5 mr. The HMS can rotate to 10.5 degrees (albeit only locally below 13 degrees), and NPS can reach its foreseen smallest angles.*

Hence, we plan to design a beam pipe with 2.5 inch diameter up to a distance of 2.35 m (beyond the slot in HMS-Q1), then flaring out to a larger diameter. This modified beam pipe assembly is illustrated in Fig. 6. It allows HMS to achieve its smallest scattering angle of 10.5°, albeit at the cost of sacrificing remote rotation for HMS below 13° or so, as the beam pipe fits snug into the HMS-Q1 slot. The modified beam pipe assembly does allow the NPS to reach its design smallest angle of 5.5° (equivalent to the smallest angle reach of SHMS) for a distance to the $PbWO_4$ calorimeter of 4 m. With this modified beam pipe assembly, we will achieve a critical angle of 13.5 mr. Note that this is the critical angle corresponding to the background simulations presented later. The general background for beam energies of 6 GeV and higher is for this beam pipe assembly dominated (90%) by the background generated directly in the beam-target interactions. Additional shielding can be considered between the beam line and the $PbWO_4$ calorimeter, near the critical distance.

For the envisioned wide-angle Compton scattering experiments, the typical angle of the NPS is much larger. For these experiments, especially as they plan to use both an 8% Cu radiator and a target, the induced bcakground in the beam line may provide a larger contributions inducing the need for additional lead shielding between the beam line and the detector. In that sense, it can be much more efficient to use a second beam pipe with increased flare or critical angle - for experiments that do not drive the smallest HMS or NPS angles we could have a beam pipe assembly with flare close to the optimal critical angle of a little beyond one degrees.

In fact, such wide-angle Compton scattering experiments drive the need for an NPS at large angles. This can be achieved by installing the NPS directly on the SHMS platform under the secondary platform for the magnet power supplies, on the right hand side (looking upstream) of the SHMS Quadrupole Magnets. In this configuration, the HB magnet still needs to be removed to make space for a sweeping magnet, and one of the stands for the magnet power supply platform needs to be removed. This is possible with the implemented design for this SHMS platform.

In Fig. 7 the proposed setup for an experiment in Hall C requiring photon or neutral-pion detection at large angles, such as wide-angle Compton scattering, is shown. With this setup, angles of up to 60° can be achieved.

D. Electron Identification and DAQ

In foreseen (e,e′π°) proposals [9], we will typically be detecting electrons with momenta ranging from ~1.5 GeV/c to about 6 GeV/c in the HMS. The HMS has a lead-glass calorimeter and a heavy-gas atmospheric Čerenkov detector for electron identification. Singles rates are typically constrained in HMS to a level of 0.5 MHz

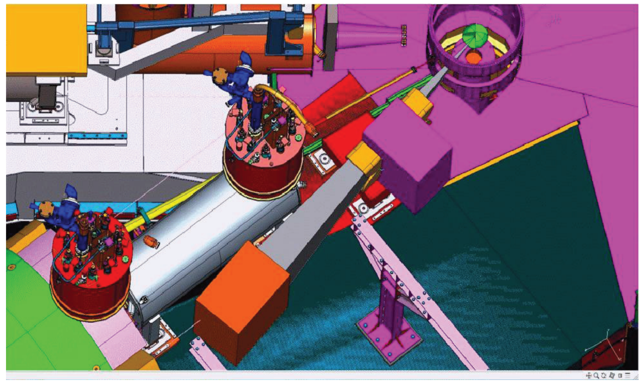

FIG. 7: *Proposed setup for a wide-angle Compton scattering (WACS) experiment in Hall C. Starting with the cylindrical scattering chamber, a sweeper magnets can be seen, followed by a vacuum channel or Helium bag, and the $PbWO_4$ calorimeter in its temperature-controlled frame. The secondary platform that holds the magnet power supplies has been removed for visualization, but the stands and supports of the secondary platform can still be seen. With this configuration, an angle range betwen ∼20° and 60° is foreseen.*

to allow for a detailed understanding of the tracking efficiency. This is not an issue for the present experiment, where HMS singles rates are expected to be less than 2 kHz (see the E12-06-104 proposal [10] for detailed single rates and π/e ratios).

A good pion/electron separation has routinely been achieved in the HMS. The current detector stack of the HMS has been shown to easily achieve e^-/π^- to $\sim 10^3$, with 98% efficiency for electron detection.

In proposal [9], the π/e ratio is never larger than 130:1. Because of the moderate pion to electron ratios, we require the events of interest to only pass some loose particle identification before generating an HMS trigger. In order to have a high efficiency for electrons, a trigger will be accepted as a true electron if either the gas Čerenkov detector has fired or if the electromagnetic calorimeter has had a large enough signal.

This will allow high electron efficiency even if one of the two detectors will have a low efficiency.

The electron trigger (ELREAL) will thus have two components: Electron High (ELHI) and Electron Low (ELLO). ELHI will require a high calorimeter signal, but no gas Čerenkov detector information, and will be composed of a high signal in the "preshower" (PRHI) and a low signal in the full calorimeter (SHLO), in coincidence with scintillator signal (SCIN).

Note that the "preshower" for the HMS is simply the first layer of the calorimeter. ELLO will require a gas Čerenkov detector signal. The final HMS trigger (COIN) will be a combination of electron (ELREAL) and sampled pion (PION) triggers, the latter requiring a standard three-out-of-four (3/4) coincidence of the x-y hodoscopes (SCIN), vetoed by a gas Čerenkov detector signal (CER).

The DAQ will record both coincidence triggers between the HMS and the neutral-pion arm, as well as single-arm HMS triggers with inclusive (e,e′) and (e,h) events. The latter will not require readout of the pion calorimeter, and the rate can be pre-scaled if necessary. However, given the low inclusive (e,e′) rates at a 1 μA beam current, we plan to include all these events in the data stream. This is important for two reasons: i) SIDIS pion multiplicities can be directly formed by taking a ratio of coincidence (e,e′π°) yields and inclusive (e,e′) yields; and ii) the inclusive (e,e′) yields will provide an additional normalization for the coincidence data.

In the off-line analysis, one can further use a cut on the coincidence timing between the scattered electron and the π°. Regular cuts on kinematic variables, such as the vertex position, the HMS collimator image, etc., can also be used to reduce any background, although likely not always needed, as requirements of the foreseen π°-detection experiments [9] are modest. For exclusive π° production, an appropriate cut on missing mass will be included to guarantee exclusivity of the p(e,e′π°)p events.

III. BACKGROUNDS AND RADIATION DOSES

A. Overview

To preserve a high and constant neutral-pion trigger efficiency during the experiment, special attention must be paid to the calorimeter radiation damage in order to avoid problems when using a high threshold in the trigger electronics. Radiation damage is determined by both instantaneous dose rate and integrated dose. The radiation dose absorbed by the calorimeter blocks at angles less than 10° is dominated by Moeller electrons.

For the $PbWO_4$ crystals such radiation effects have been tested in HEPI (Protvino, Russia), at Brookhaven National Laboratory, and at CERN. At low dose rates (15-20 krad/h or less), and at integrated doses below 10 krad only a 2-3% degradation effect of $PbWO_4$ was observed [11].

The radiation damage dramatically increases at higher doses. For example, at a dose rate of 100 krad/h the radiation damage amounts to roughly 5% degradation, while the crystal degradation reaches 10-25% [11, 12] at a dose rate of $\sim$500 krad/h and integrated dose of 1-2 Mrad.

Without exceptions, in all cases the loss of resolution is attributed to degradation of the transmission properties of the blocks, and not to the degradation of the photocathode of the PMTs.

The simulated total dose rates amount to 274 rem/h when averaged over an angle of 5-25 degrees, and calculated for a 1 μA beam current, a 10 cm long cryogenic hydrogen target, and a beam energy of 6.6 GeV. We have verified that the background rates only slightly depend on the beam energy, with simulations at 6.6 and 11 GeV agreeing at a better than 20% level. A 7.5 kG sweep magnetic field reduces these dose rates to 18 rem/h. The dose rates fall rapidly as the angle increases from 5 to 25 degrees, by approximately one order of magnitude, and are, as expected, dominated by (Moeller) electrons. At 5.5 degrees, the dose rates correspond to 400 rem/h (without field) and 50 rem/h (with field), respectively.

Given that we anticipate only limited kinematics close to this smallest angle of 5.5°, with more typical kinematics at $\sim 8^\circ$ and beyond, the dose rates look modest and certainly easily acceptable for a 1 μA beam current assumption and the proposed sweeping magnet. In addition, we have prepared and tested custom pre-amplifiers in order to operate the PMTs at lower high voltages, with lower anode currents.

More details on the rate simulations and the modified voltage divider design can be found in sections III B and III D. We come back in details to the anticipated radiation dose effects and allowable radiation doses by the improved setup in sections III E and III F.

B. Electromagnetic Background Simulations

We will use $PbWO_4$ blocks similar to the inner high-resolution part of the Hybrid Electromagnetic Calorimeter (HYCAL) [4] for the detection of the photon-pairs from π° decay. The HYCAL calorimeter has previously been successfully used in JLab's Hall B PRIMEX and PRIMEX-II experiments, to precisely measure the neutral pion's lifetime. Energy and coordinate resolutions of $\sigma/E = 1.3\%$ and $\sigma_x \sim$1.28-2.10 mm have been achieved at a neutral-pion energy of 5 GeV.

For the envisioned small angles the neutral-pion detector will operate at high rates, and associated high radiation dose. In such conditions, the $PbWO_4$ crystals can accumulate doses that would damage their transmission properties. This would result in a loss of energy resolution of the calorimeter, which in turn worsens the missing mass resolution. Special attention must be paid to the detector background condition.

The background rates and the NPS radiation doses (for now without the effect of the sweeping magnet included) have been calculated by Pavel Degtiarenko [13]. The various particle rates as a function of angle and particle energy as induced by the interaction of a 6.6 GeV electron beam and a 10 cm liquid hydrogen target are shown in Figs. 8 and 9, for photons, positrons, electrons and positively-charged pions, as examples. These rates are for a 1 μA beam current and a 10 msr solid angle detector.

Given the strong angular dependence of background rates, we only show the rates and radiation doses for angles smaller than 20° in Figs. 8 and 9. Rates at larger angles are completely negligible compared to this.

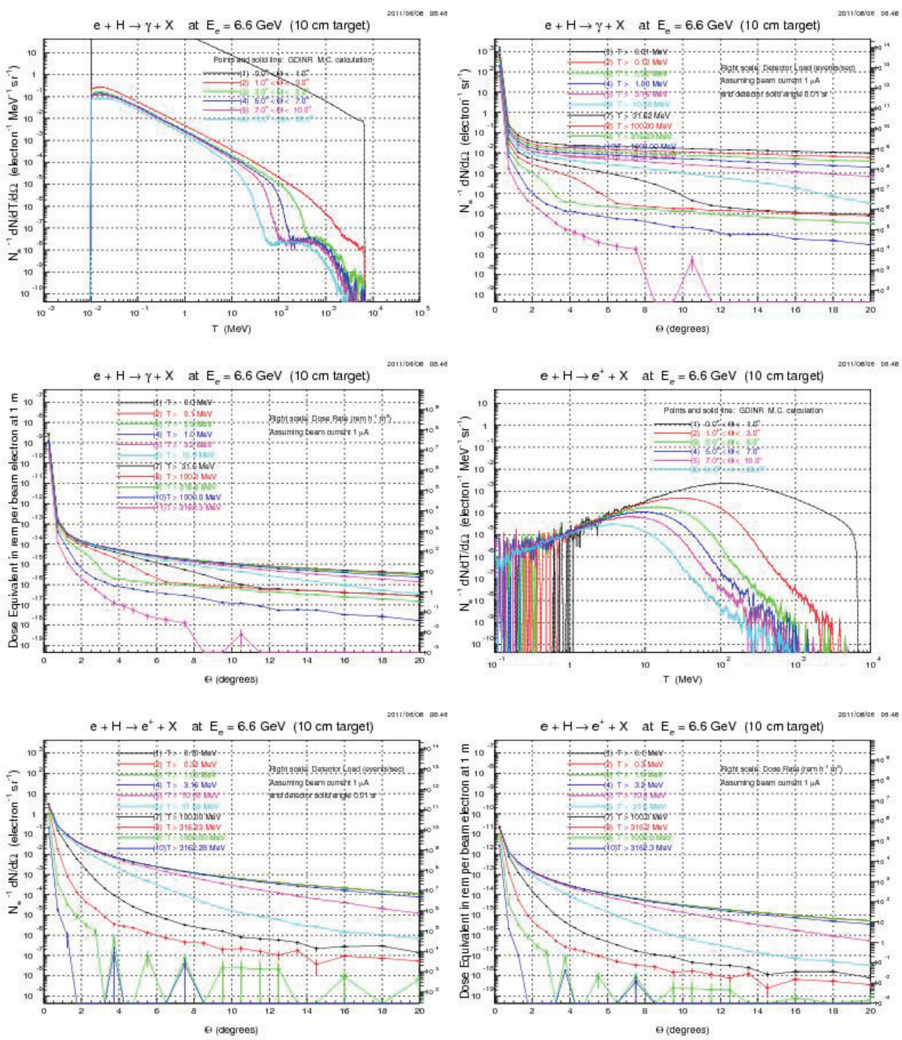

FIG. 8: Expected particle background rates and the radiation dose as seen by a 10 msr detector for photons and positrons, assuming a beam energy of 6.6 GeV, a beam current of 1 μA, and a 10 cm LH2 target.

This strong angular dependence is further highlighted in Table II, which shows the estimated rates (events per second) for photons, electrons and positrons for a detector with solid angle of 10 msr positioned at 3.5, 6.0 and 8.5 degrees, respectively.

Taking into account that we plan to use a $\sim$1000-channel lead-tungsten calorimeter with a solid angle of about 25 msr, the particle rates will be higher by factor of 2.5, resulting in a rate per crystal of over 2 MHz for angles $\leq$6 degrees, with the major fraction of the rates produced by Moeller electrons. It is obvious that the use of a magnet to sweep these electrons is essential.

Fig. 10 shows the layout as used in the simulations. It includes the 10 cm LH2 target located inside the 12-GeV-compatible existing Hall C scattering chamber. The mechanical dimensions of the HB magnet with its bore are used to indicate the yoke and position of the sweeping magnet, bending electrons inwards (towards smaller angles). Here, a 7.5 kG magnetic field is simulated, corresponding to 0.3 Tm. The front face of the detector is at a distance of 4 meter from the target, and covers in this layout an angular range between 5 and 25 degrees. The black dashed-dotted lines correspond to angles of 3, 5, 15, 25 and 28 degrees, respectively. The red

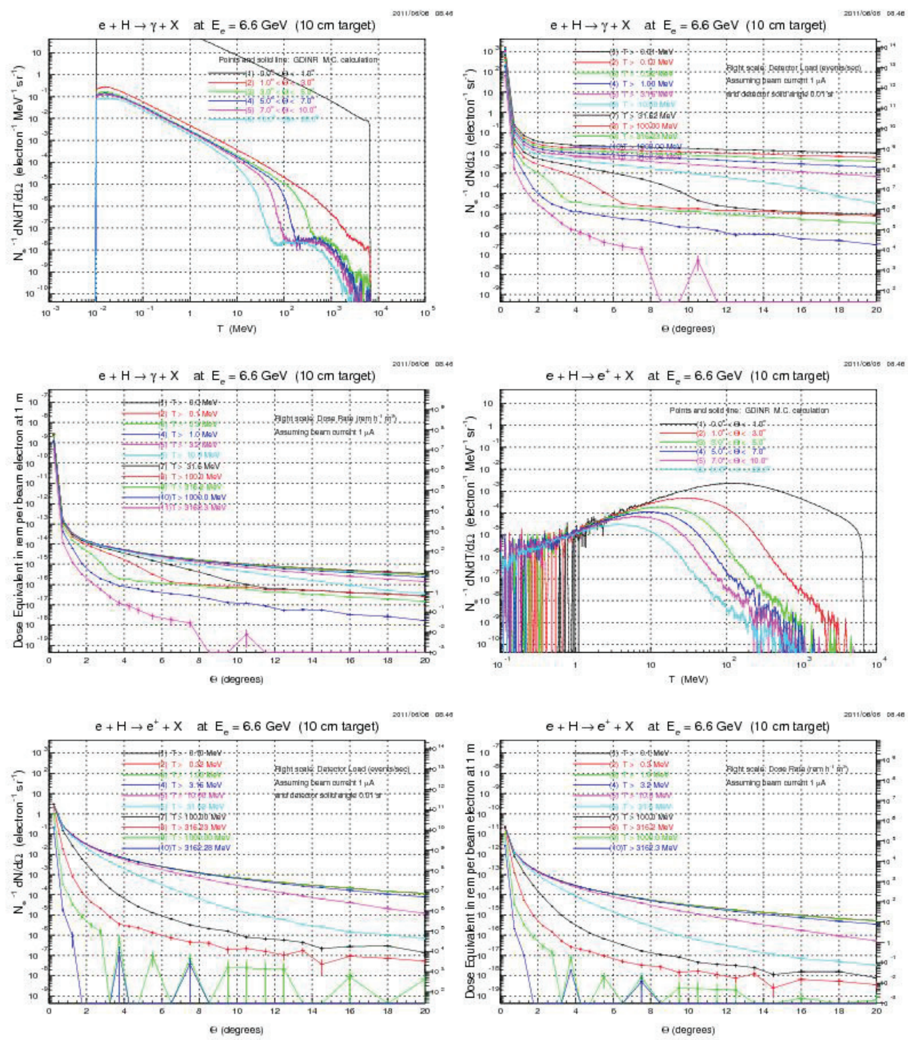

FIG. 9: Expected particle background rates and the radiation dose as seen by a 10 msr detector for positrons and π^+, assuming a beam energy of 6.6 GeV, a beam current of 1 μA, and a 10 cm LH2 target.

track shows the trajectory of a 500 MeV electron emitted at an angle of 15 degrees. We note that the 0.2-0.3 Tm design requirement of the sweeping magnet is driven by guaranteeing sufficient bending power to sweep away up to 300 MeV electrons. This has a tremendous impact on the particle rates shown earlier in Fig. 9 (top right panel).

Figs. 11(a) and 11(b) further show simulated trajectories for 10000 beam-electrons with an energy 6.6 GeV, with the sweep magnetic field "OFF" and "ON", respectively. Blue and red tracks correspond to photons and charged particles, respectively, and the "cleaning" effect of the sweeping magnet can be readily seen.

To quantify the effects of the sweeping magnet further, the results of the dose rate calculations (in rem/hr) for a 1μA beam current and a 6.6 GeV beam energy, with a 7.5 kG magnetic field (0.3 Tm) OFF and ON are presented in Table III. We note that the presented results are *averaged* over the 5-25° detector front face. The dose rates fall rapidly as the angle increases from 5 to 25 degrees, by approximately one order of magnitude. At 5.5 degrees the dose rates correspond to ∼400 rem/hr for the field OFF, and ∼50 rem/hr for the field ON

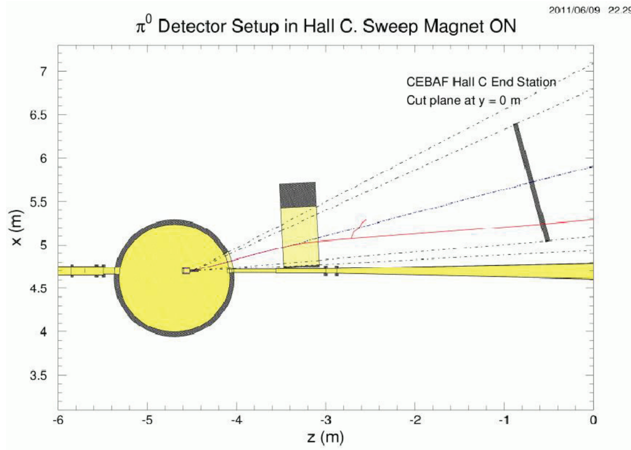

FIG. 10: The schematic layout of the sweep magnet.

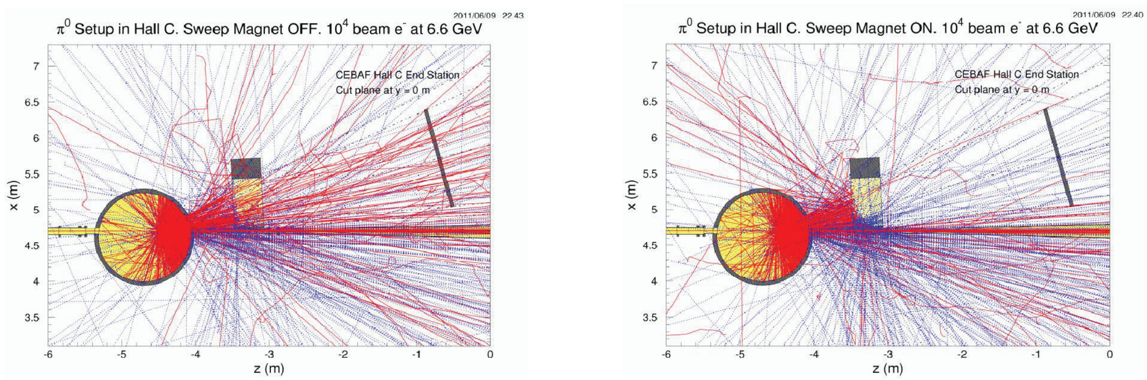

(a) (b)

FIG. 11: *(a): Simulated trajectories for 10000 beam electrons with an energy of 6.6 GeV, with the sweeping magnet OFF.(a) and ON (b) configuration*

configuration. The latter looks certainly acceptable.

We further illustrate the results of detector count rates as simulated with the well-calibrated GEANT3 code used for successful execution of all JLab experiments in Fig. 12. The six panels correspond to three different energy thresholds each, with the sweeping magnet both ON (left panels) and OFF (right panels). The flux is in the Hz/cm^2 units, at the front face of the neutral particle detector and is a function of the position horizontally along the detector, and away from the beam line. The bin sizes correspond roughly to steps of one degree in the scattering angle.

Particle	$3.5°$	$6.0°$	$8.5°$
Electron	3×10^9	6×10^8	6×10^6
Positron	6×10^6	6×10^5	2×10^5
Photon	4×10^8	2×10^8	1×10^8
Total	3.4×10^9	8×10^8	1×10^8

TABLE II: Particle rate (event/sec) for a detector with solid angle of 10 msr located at an angle of 3.5, 6.0 and 8.5 degrees, respectively. These rates assume a beam energy of 6.6 GeV, a beam current of 1 μA, a 10 cm long LH2 target, and no sweeping magnet.

	Magnet OFF	Magnet ON
Photon dose rate	3.03±0.03	2.81±0.03
Positron dose rate	5.43±0.13	3.75±0.11
Electron dose rate	265.23±0.95	11.48±0.23
Total dose rate	273.69±0.96	18.04±0.26

TABLE III: Simulated dose rate (rem/hr) for a 1 μA beam current and a 6.6 GeV beam energy, with a 7.5 kG (0.3 Tm) magnetic field OFF and ON. The errors are purely statistical and somewhat underestimated as a Gaussian approximation has been used for a distribution that is significantly non-Gaussian.

With the magnetic field added, the dominant source of the background rates now become photons with an energy above 10 MeV and electrons with an energy above 100 MeV. As one would have anticipated, the use of a relatively simple sweeping magnet will dramatically reduce the (Moeller) electron rates. At the smallest angles foreseen, the rate of photons with energies $E_\gamma > 10$ MeV is $N_\gamma \sim 3 \times 10^5$ Hz/cm^2. For $PbWO_4$ crystals with dimension of 2.05×2.05 cm^2, the photon rate per crystal is $\sim 1.2 \times 10^6$ Hz. The electron rates with energy $E_e >$100 MeV is $N_e \sim 6{\times}10^5$ Hz/cm^2, or $\sim 2.5{\times}10^6$ Hz/crystal without sweeping field, and drops to $N_e \sim 5{\times}10^4$ Hz/cm^2, or $N_e \sim 2 \times 10^5$ with sweeping field. This shows the sweeping magnet has, as designed, also still quite some impact on electrons with energy above 100 MeV.

In Fig. 13(a) and Fig. 13(b) we show the flux of photons, electrons and positrons as determined from the detailed numerical results underlying the expeeted background rates in Figs. 8 and 9, for a photon threshold energy of 10 MeV and an electron (or positron) threshold energy of 100 MeV. The $PbWO_4$ detector is asumed to be at a 4 meter distance from the target, and cover a solid angle of 10 msr. Note that this is smaller than the envisioned $PbWO_4$ detector, but this will be taken into account later. Each $PbWO_4$ crystal has a 2.05 by 2.05 cm^2 size, and covers a solid angle of 0.025 msr. The 10 msr case corresponds to the top panels of Fig. 13(a) and 13(b), the single $PbWO_4$ crystal case corresponds to the bottom panels. The flux is shown for two cases, without and with a sweeper magnet (Sweep OFF and ON), in Figs. 13(a) and 13(b), respectively.

In Fig. 14 we illustrate the photon flux, for the sweeper magnet on situation, but as a function of the photon energy threshold ranging from 1 to 100 MeV. As anticipated, the flux drops with angle increase. For higher thresholds, the drop can be initially very fast at smaller angles, and more graduall at larger angles. This is due to the drop of the electron flux generating the photons. For instance, the photon flux can drop by a factor of ∼100 for the energy range from 0.5 to 200 MeV, thus higher thresholds will give drastically reduced fluxes.

The major sources of the background were found to be the target-induced rates, with the induced background from beam line componets contributing perhaps 10-20%. We did verify that the background conditions for an 11 GeV beam energy are nearly similar to a 6.6 GeV beam energy, through are overall some 10% smaller for all angles. Thus, all the background rates given for the 6.6 GeV beam energy give a very good representation of an 11 GeV beam energy too.

C. Detector Linearity and Efficiency

Studies have shown that detector performance (particularly the PMT gain) may change by few-percent to few-tens-of-percent level for a high flux (at dose rates > 1 Rad/hr). The scale of this change of performance depends on the type of crystal, the PMT and on other components of the hardware.

Two types of $PbWO_4$ crystals, SIC and BTCP, have shown opposite behavior in the detector response above dose rates equivalent to 4 GeV electrons at ∼ 50 kHz in an early low-current electron beam test of the PRIMEX collaboration [14]. This behavior could be caused by three effects:

- change of the scintillation mechanism in the crystals;
- change of the light transmission in the crystals;
- change of the PMT gain due to rate variations.

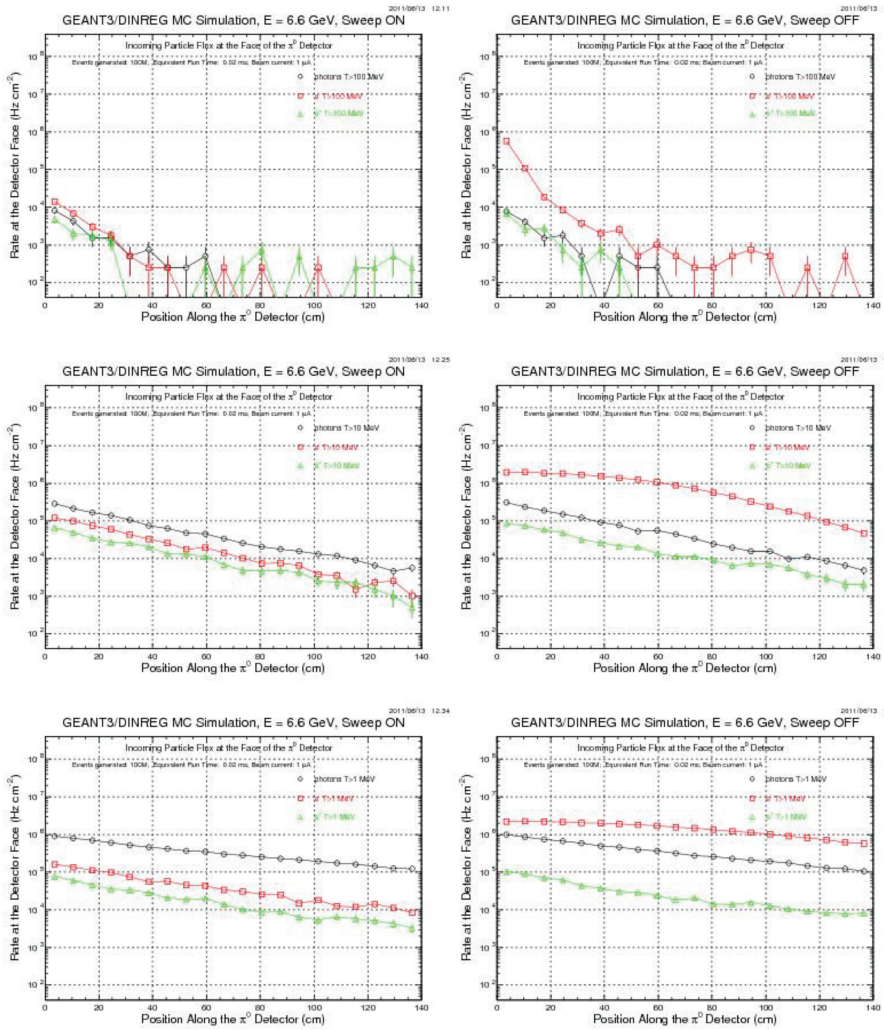

FIG. 12: Simulated flux of the particles (in Hz/cm^2) at the face of the detector as a function of the position (in cm), at three energy thresholds (from top to bottom 100, 10 and 1 MeV) and with the sweeping magnet ON (left) and OFF (right).

The results of the PRIMEX studies of the PMT gain variation with rate are presented in Fig. 15.

The overall variation of the measured signals relative to their values at modest rates (for 4 GeV electrons) was found to be small, $\pm 1\%$, up to rates of about 10^5 Hz. Beyond such high rate, deviations grow fast, which is understandable as such a high rate will require a PMT with a fast response, operated at low gain and low anode current. The construction and use of custom pre-amplifiers to allow operation of the PMTs at lower high voltages, and to compensate the gain reduction, will offer a solution for high rates. We will describe such modification and subsequent performance tests later.

The loss of amplitude is considered to be due to degradation of the transmission properties of the blocks, but not because of degradation of the photo-cathode of the PMTs. Hence it is possible to cure any radiation damage by exposing the $PbWO_4$ crystals to near-UV blue light. A continuous monitoring of the crystal performance through physics measurements (like elastic $e-p$ scattering, or π° mass reconstruction) can be considered, if possible, and, pending on the experimental situation curing cycles can be integrated. We estimate such a curing

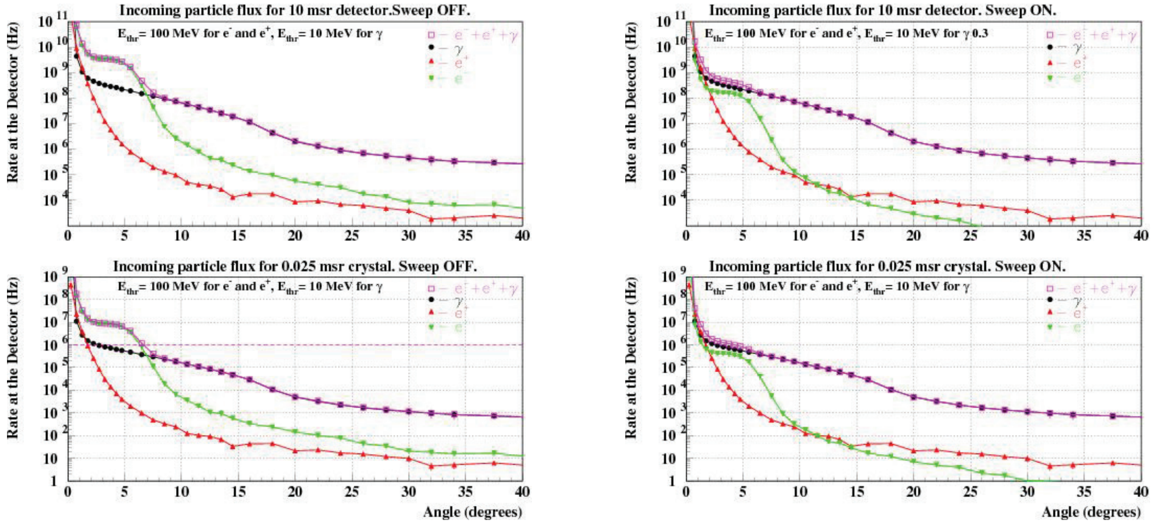

(a) (b)

FIG. 13: *The flux of the particles for the 10 msr detector and 0.025 msr single crystal as a function of the angle at energy thresholds 10 MeV for photons and 100 MeV for electrons and positrons. The detector (crystal) is at the distance of 4 m from the 10 cm LH2 target. The beam energy and current are 6.6 GeV and 1.0 μA. The sweep magnet is OFF (a) and ON (b).*

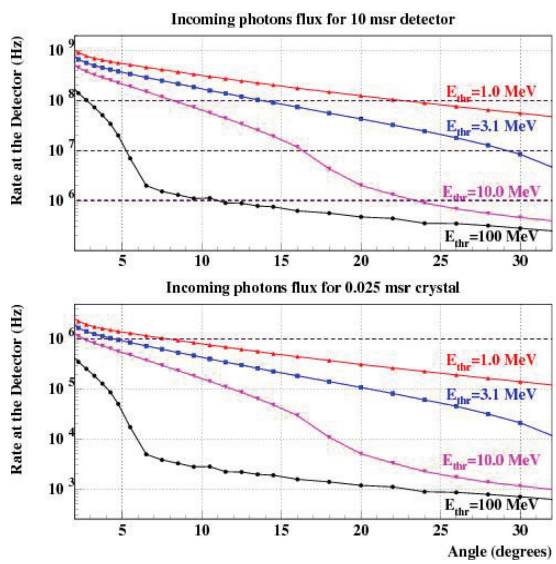

FIG. 14: *The flux of the photons of the 10 msr detector and 0.025 msr single crystal as a function of the angle at energy thresholds 1.0, 3.1, 10 and 100 MeV. The detector (crystal) is at the distance of 4 m from the 10 cm LH2 target. The beam energy and current are 6.6 GeV and 1.0 μA.*

cycle to require in general a shift. It may well be possible to do such a curing cycle during an opportunistic beam studies or beam down times.

As is described in more detail in section III B, the main source of background in the detector is low-energy photons. In the worst-case scenario (central angle of about 5.5°), the background rate is expected to be 200 MHz within the calorimeter acceptance, or on average 200 kHz per module. These rates are under the assumptions of 1 μA beam current impinging on a 10 cm LH2 target, with high (6-11) GeV beam energies and with the

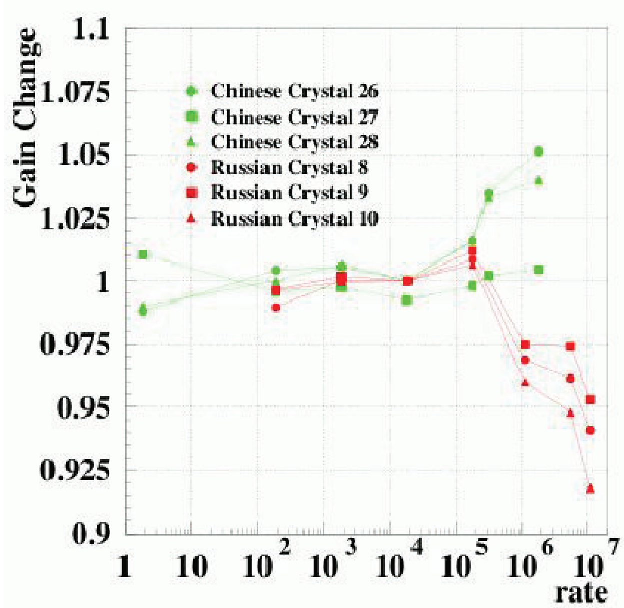

FIG. 15: The variation of the PMT gain for two different types of $PbWO_4$ crystals as tested for the PRIMEX apparatus, as a function of the rate induced in a low-current electron beam test. (Adopted from [14]).

$PbWO_4$ detector at a distance of 4 meters. Of course, the rate of the background is not uniform, and will in this worst-case scenario be a factor of 2-4 higher for the crystals closest to the beam line, at about 3.5°. The dominant fraction of these photons has energies below 10 MeV, which is in order of the critical energy of 8.5 MeV, where ionization and Cherenkov radiation losses are equal. But, these low-energy photons can still cause pile-up and additional anode current.

The latter is not a real issue, as shown in Fig. 16, which shows that the PMT gain variations can be controlled to better than 1% at up to 1 MHz rates per crystal if one abandons the PMT base design of the PRIMEX experiment and rather adopts a modified PMT base design [15]. The new modified active base design gives a factor of ∼25 improvement in gain stability over the existing PRIMEX bases. The tests and base modifications are described in detail in Section III D.

Given that we ultimately expect linear gain over the anticipated rates of the $PbWO_4$ crystals, the photon background will act solely as an energy baseline shift. We will use the exclusive ^{1}H(e,e$'\pi^\circ$)p reaction here as an example to show the impact on expected detector stability and hence systematic uncertainties. First recall that in such an experiment we can overdetermine neutral pions both from the measured energy and the decay angle. Second, if we can reduce the background rates, the baseline shift will become less important and will be actually small even within a 100 ns gate. Assuming an average photon energy of 10 MeV, the rates mentioned above, and a few crystals firing for each decay photon shower, we would get a baseline shift of less than 10 MeV in a 100 ns gate. This is well within the expected energy resolution of the $PbWO_4$ crystals for photons associated with some 2-5.5 GeV (or higher energy) neutral pions.

Details on the performed rate simulations were already given in section III B. Given an average background rate of well below 1 MHz per crystal, and maximum rate of 1 MHz in the crystal closest to the beam line for a neutral-pion setup at a worst-case minimum angle of 5.5°, we conclude that the gain is stable to about 0.2% for all anticipated kinematics and background conditions (assuming here again a 1 μA beam current impinging on a 10 cm LH2 target). One can scale to different conditions.

As in the PRIMEX experiment, we have included a temperature-stabilization system in the design, hence contributions to gain stability due to temperature dependences are small, <0.2% (a 0.1°C temperature stability guarantees a 0.5% energy stability for absolute calibration and resolution).

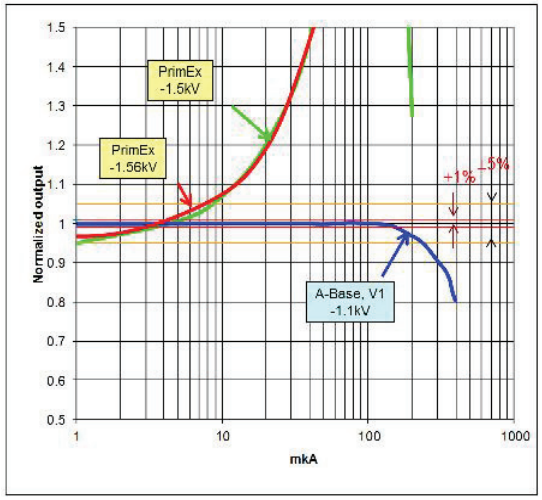

FIG. 16: *The PMT gain stability as a function of anode current. The thin solid red horizontal lines denote stability to 1% and the yellow solid lines stability to 5%. The new active base design A-Base [15], V1 outperforms the PRIMEX bases by a factor of about 25.*

Earlier we have shown the combinatoric background to be also small, <1%. We likely will know this background to a fraction of %. Nonetheless, since the background conditions change with angle, we conservatively assign an uncertainty of about 0.2-0.5%.

Lastly, the uncertainty in the geometric acceptance is correlated with the knowledge of survey and actual beam position, but will be well known (<0.1%). Overall, we feel we can achievably assume the the detection efficiency for this example of π° experiment to be stable to <0.5%.

D. Test Results for R4125 Photomultiplier Tubes with Active Bases

To increase the gain stability at the high rates anticipated with the NPS setup we have redesigned the R4125 photomultiplier used for the $PbWO_4$ crystal readout during the PrimEx experiment to have an active base. Here, the amplifier was powered from a high-voltage division chain. An initial "V0" base was tested by using a 5 mm^3 cube of Pr:LuAG scintillator to simulate a light pulse wave form similar to that of a $PbWO_4$ crystal, albeit with a factor of 200 more light output. This setup allows to simulate light corresponding to a few hundred of MeV energy deposited in $PbWO_4$ using common gamma sources. The setup was equipped with an LED diode to map the gain dependence as function of anode current. Results were encouraging, and a large gain factor ($\sim$ 25) was established with respect to the Primex existing base.

Nonetheless, these test results of the first prototype still showed a problem similar to the behavior of the original PRIMEX base, in that both base circuits use a simple passive division and are sensitive to the anode current. The tube gain then varies as function of anode current (or equivalently count rate), which could introduce a rate-dependent gain modulation. This effect is related to the current drain from the last dynodes of the division chain. It was compensated by equipping the base with two transistors connected to the last dynodes, and stabilizing the voltage on dynodes 9 and 10. The divider drain current and division ratio remained unchanged. Fig 17 shows the modified High Voltage division chain, termed the "V1" base.

The count rate capability of the modified base circuit was tested with a double LED setup.One of these LEDs was powered from pulse generator, whereas the second LED was connected to a regulated DC current source. The LED light pulse shape was tuned to $\sim$18 ns FWHM, mimicking a scintillator pulse shape and similar to the pulse shape of the original PrimEx base (see Fig. 18(a)). In Fig 18(b) we show the High Voltage base design which was used in the PrimEx experiment (top) and the modified active base (bottom).

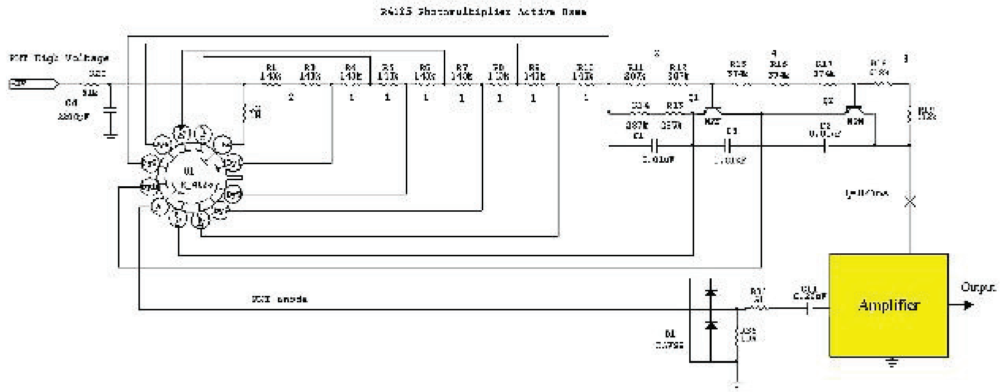

FIG. 17: *R4125 Photomultiplier tube active base circuit diagram. Two (Q1, Q2) high voltage transistors are added to the last two dynode (9 & 10) power connection nodes.*

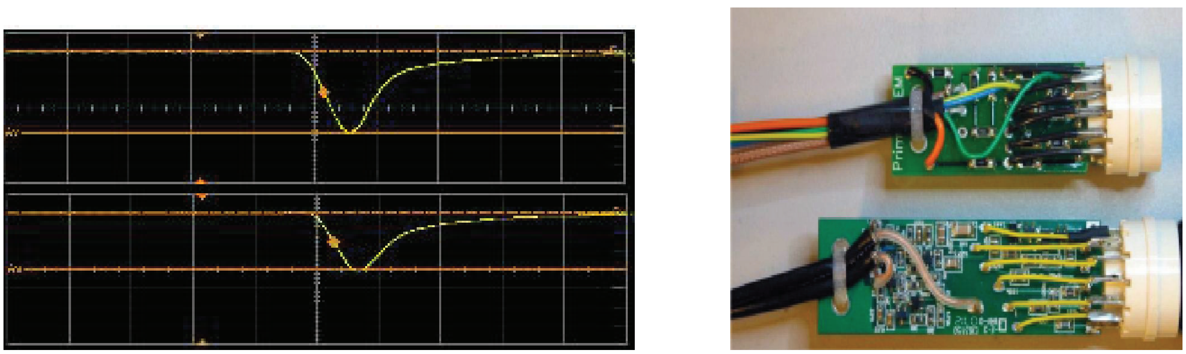

(a) (b)

FIG. 18: *(a) LED pulse waveforms recorded from the original PrimEx (top image) and the redesigned active base (bottom image). The horizontal scale is 20 ns per division, the vertical scale is 100 mV per division, for both images. Both records are acquired at 10 kHz LED pulse frequency. (b) Design of passive base (top) used in the PrimEx and the new active base (bottom) developed by V. Popov [15].*

The high-voltage bias was -1.1 kV for the new active base, where it was -1.56 kV for the original PrimEx base, to maintain about 300 mV output pulse amplitude for both PMT bases. The passive base output current is not different from the anode current, while the active base effective output current is about 10 times higher. Fig. 16 presents the summary of our tests. The results obtained from testing of our first version "V0" base (without transistors in the division chain) are included. Note that we find the gain function as function of anode current for the PrimEx bases to be consistent with either technique: using a scintillator with gamma source and measuring the photo peak, or using the LEDs either by pulsing of DC power source.

The active base design can be seen to have improved gain stability with an efficient output signal range up to $\sim 160\ \mu$A. In this range, the PMT base system gain, or pulse amplitude and pulse width, remain stable to within 1%. The measured pulse rate at this current corresponds to a rate of about 1.2 MHz of 300 mV output pulses. The PrimEx base during the test with the same LED light pulses on the other hand has a noticeable strong PMT-and-base system gain dependence as function of count rate (or anode current). With the same LED light setting, the original PrimEx PMT/base is running out of a $\pm 5\%$ gain stability range at a count rate of $\sim$ 30 kHz. The maximum anode current for linear operation of the active base has not changed, being proportional to the divider drain current which remains the same. Table IV summarizes the comparison between the various PMT bases.

In summary, the total count rate advantage of the newly designed active base remains unchanged between

TABLE IV: *Comparison of the original PrimEx base (and accompanying PMT) with the modified "V1" active-base design.*

Parameter	PrimEx Base	"V1" active base
Maximum anode current	$\sim$6μA, gain variation $\pm$5%	$\sim$16μA, gain variation $\pm$1%
Maximum output pulse	unknown	-4 V, (-80 mA/50 Ohm)
Divider current	170 μA at 1.5 kV	450 μA at 1.1 kV
Maximum linear count rate	30 kHz $\pm$5%	1.2 MHz $\pm$1%

the "V0" and "V1" versions: a factor of $\sim$ 25 as compared to the PrimEx base. However, as compared to both original PrimEx base and earlier passive-divider "V0" base, the "V1" active-base design indicates a noticeable improvement of the gain stability of the complete PMT plus base system versus count rate.

As a final test, we also performed radiation tests of the active PMT base in Hall C during the Qweak operations in 2012. We have found no degradation of the base for a radiation dose of 100 kRad. Hence, we plan to build, test and use such active bases for all $PbWO_4$ crystals of the planned Neutral-Particle Spectrometer.

E. Radiation Effects

Nearly all the known crystal scintillators are sensitive to electromagnetic and hadronic radiation. Interaction of ionizing radiation with scintillation crystals creates radiation damage. The creation of radiation damage involves impurities and defects in the crystal. Accumulated radiation at high doses may significantly change their characteristics. The most common damage is radiation-induced light absorption or change of crystal transmittance caused by the formation of color centers. Radiation may also cause reduction in the scintillation light yield (damage of the scintillation mechanism), and, because the radiation dose may not be uniform, a change in the light response uniformity.

Studies show that the degradation in optical transmission is the most important effect of radiation damage. In most crystals, the observed loss in scintillation light output can be explained by a decrease in transmission. Therefore, the radiation hardness studies always first refer to measurements of the optical transmission of a scintillator irradiated by various types and doses of radiation.

Radiation damage is determined by both the instantaneous dose rate and the integrated dose. Within an electron scattering environment, the generated radiation doses, and thus those absorbed by any calorimeter crystals, at angles less than 10° are dominated by Moeller electrons and related Bremsstrahlung.

$PbWO_4$ is known as a fast, dense and highly radiation resistant scintillator. Hence, it was for instance selected for construction of electromagnetic calorimeters for the CMS, ATLAS, and ALICE detectors operating at the LHC at CERN. For $PbWO_4$ crystals, radiation effects have been tested in HEPI (Protvino, Russia), at Brookhaven National Laboratory, and at CERN. A radiation hardness study of $PbWO_4$ crystal blocks intended for the BTeV experiment [16] showed that the radiation damage indeed depends on the dose rate (Rad/unit of time) for crystals irradiated by pure, intense high energy electron and hadron beams, as well as by a mixture of hadrons, neutrons and gammas.

The dedicated radiation dose studies showed that the $PbWO_4$ crystals degraded only by 2-3% for low dose rates, 15-20 krad/hr or less, and integrated doses below 10 krad [11]. Radiation damage dramatically increases at high doses. For example, while at a dose rate of 100 krad/hr the radiation damage amounts to $\sim$ 5%, the crystal degradation can reach 10-25% at instantaneous dose rates of $\sim$ 500 krad/hr and integrated doses of 1-2 Mrad [11, 12]. Without exceptions, the loss of resolution is attributed to a degradation of the transmission properties of the crystals themselves, and not to the degradation of the photocathode of the PMTs.

Clear observations of the degradation of the light output as a function of dose have been reported in several papers. Nearly all the studies agree that at any given dose rate, after some irradiation time the degradation effects saturate. The level of the degradation scales with the dose rates. As an example, in Fig. 19 we show the results of a group at CMS [26]. For Nb/Y-doped $PbWO_4$ crystals, they measured the light output as a function of irradiation time for varying dose rates: 15, 100, 500 and 1000 rad/h. The light output was normalized to that before irradiation.

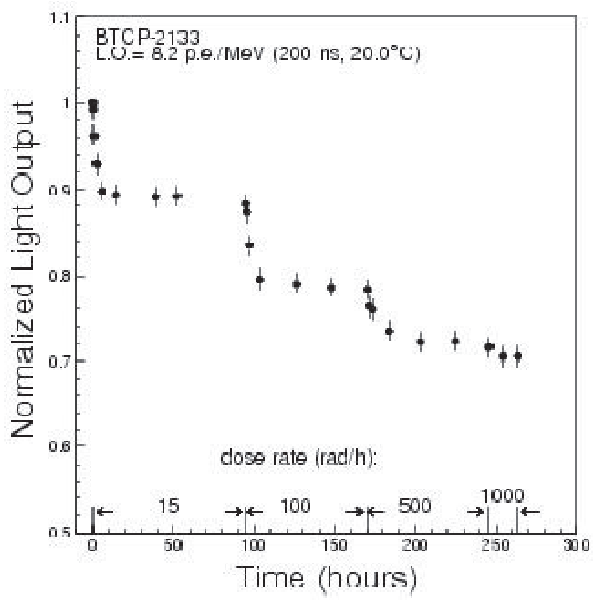

FIG. 19: *Light output as a function of irradition time for dose rates of 15, 100, 500 and 1000 rad/h, for a sample of Nb/Y-doped $PbWO_4$ crystals from BTCP. (Adopted from Qu Xiangdong Ph.D. Thesis [26]).*

A clean saturation behavior of the degradation effect can be seen for each of these dose rates. For this particular $PbWO_4$ crystal and a dose rate of 15 rad/h, a fast degradation of the normalized light output of $\sim$10% can be seen. The degradation then remains unchanged for the next 100 hours of radiation. After the radiation dose is changed from 15 to 100 rad/h, the light yield drops another 10% making the total degradation effect $\sim$20%, and then remains at this level for the next 70 hours of exposure. This pattern repeats with the next changes in radiation dose, from 100 rad/h to 500 rad/h, and finally to 1000 rad/h, although drops in light yield become less. Although the scale of degradation varies from crystal to crystal and depends on radiation dose, the behavior shown is common. Thus, careful studies and tests of samples of $PbWO_4$ with varying impurities, types and amount of doping materials are needed to select the proper crystals given particular radiation conditions and exposition times.

To improve the radiation resistance of the crystals usually they are doped with a small amount (40-100 ppm) of Nb, La, Lu, Y, Gd, Al or Ce at different stages of the growth process. Pentavalent Niobium (Nb) doping in $PbWO_4$ was first reported by Lecoq *et al.* to be effective in improving the transmittance at a level of 100 ppm [5]. Trivalent Lanthanum (La) doping was reported by Kobayashi *et al.* to be effective in improving transmittance and radiation hardness [27]. These pioneering studies were followed by studies with various other ions and their combinations, to further improve optical quality and radiation resistance of the crystals [5, 28, 29]. Perhaps not surprising given this situation, measurements indicate that $PbWO_4$ crystals produced by different manufactures may have significantly different properties, depending on the concentration and type of doped impurity.

The background radiation was further found to have strong negative impact on the optical properties of the crystals. Effects of this radiation damage again depend on the dose rate, the integrated dose, and the type of particles casuing the dose. At doses of more than 100 krad ($>$ 1 kGy), clear differences in the light transmission characteristics of the crystals exposed to protons have been observed as compared to photons. In proton-irradiated crystals, the band-edge (in light transmission versus wave length) shifts towards longer wavelength, while this band-edge remains stable in photon-irradiated crystals. Photon-induced damage saturates after a few hours of exposure at a dose rate of ∼100 krad/h (1 kGy/h), while proton-induced damage increases linearly [24]. In addition, hadron irradiation may cause the crystals to become radioactive (due to the creation of nuclear fragments).

The transmission for samples of $PbWO_4$ crystals both before and after an integrated dose of 2 Mrad was measured in [17]. The results are shown in Fig. 20, and indicate only a ∼15-20% degradation in the wave length range of λ ∼350-400 nm, even at such a high integrated dose. Zhu *et al.* [18] studied the effect of integrated radiation dose for the $PbWO_4$ crystal for the LHC detectors, where dose rates of $\sim 15-500$ rad/h were expected. They reported that for $PbWO_4$ crystals the light output and slope did not show change up to an integrated dose of ∼2.2 Mrad (see Fig. 21). Similar results were observed in studies of the CMS Electromagnetic Calorimeter Group [19]. Comparison of luminiscence spectra measured both before and after an 100 krad photon irradiation (with a dose rate of ∼3.5 krad/hr) did not show any changes or damage to the scintillation mechanism.

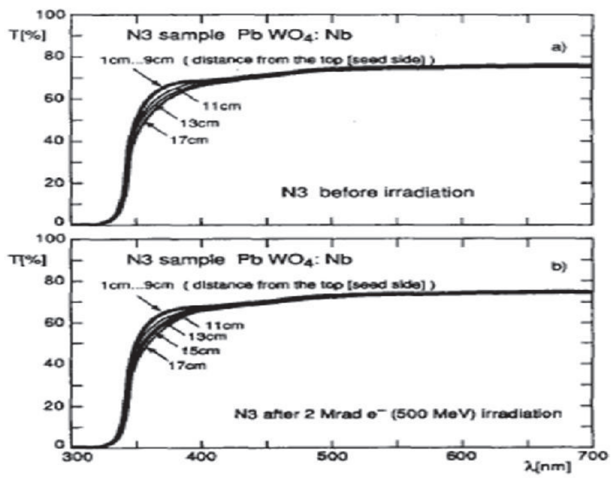

FIG. 20: *Transmission for samples of $PbWO_4$ crystals both before and after integrated doses of 2 Mrad. (Adopted from A. Fyodorov et al. [17]).*

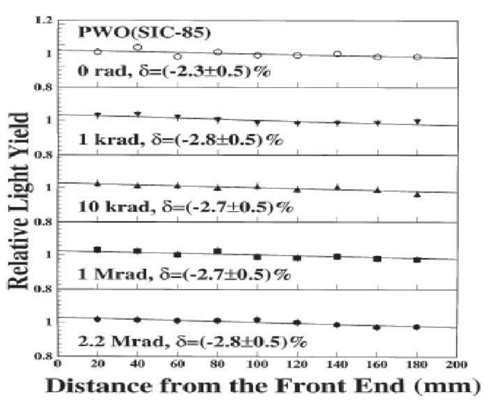

(a)

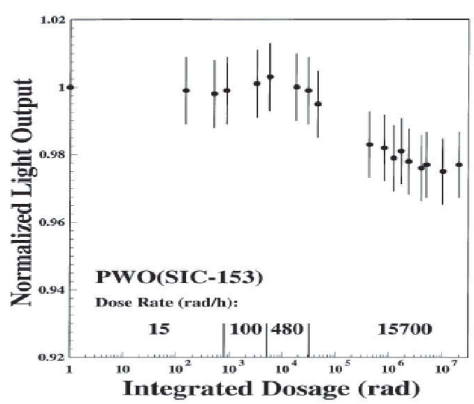

(b)

FIG. 21: *(a) The light response as a function of distance from the front end of the crystal at different integrated radiation doses. (b) The normalized light output of a $PbWO_4$ crystal as a function of integrated dose. (Adopted from [18]).*

These results confirm that the scintillation mechanism is not damaged, and possibly only the front (few cm) of the crystals was subject to the radiation dose. A threshold behavior of radiation damage was observed, *i.e.* only particles above a certain energy appear to cause damage. For instance, the radiation damage due to fast hadrons seems parameterized in terms of their inelastic interaction rate, rather than the hadron flux. Since the crystal contains heavy elements, fast hadrons (above ∼20 MeV) will produce heavy fragments. The energy loss of these slow fragments will amount to ∼50000 times those for minimum-ionizing particles.

Low energy neutrons (<20 MeV) do not cause significant damage to the crystals. The effect of an intense neutron flux on $PbWO_4$ crystals was studied in nuclear reactors (see Ref. [20], [21] and [22]). No significant effect was found up to flux densities of 10^{14} $cm^{-}2$. Even at very high neutron fluxes, of the order of $10^{19} - 10^{20}$ neutrons/cm^2, and extremely high doses of 330 MGy (33000 Mrad), the $PbWO_4$ crystals remained scintillating [23].

Some irradiated crystals can naturally recover transmission with time, at room temperature. However, such recovery is very slow, especially in the short wavelength region. The damage in $PbWO_4$ is thermally annealable, as well as optically bleachable [25]. For most of crystals almost complete recovery in transmission can be obtained after thermal annealing at temperature 200-500^o C.

A more suitable way of recovery is optical bleaching by ultraviolet (UV) or visible light. Such recovery is very effective for all crystals and can be implemented in situ. Almost full recovery in the transmission can be reached after exposure to light, ranging from tens of minutes to several hours, all depending on the intensity of the light source at a specifically selected wavelength. Even after multiple recovery the light yield and timing properties of the crystals remains nearly unchanged, and similar as for a non-irradiated crystal.

F. Radiation Doses

Radiation dose rates from Pavel Degtiarenko's realistic background simulation have been used to estimate the exact radiation condition as seen by the $PbWO_4$ detector as part of the NPS facility. We take into account the major sources of radiation: photons, electrons and positrons (since neutron radiation is moot, see the previous Section).

On the right hand side of the earlier presented particle background rates, a scale is added to indicate the radiation doses for a detector at a distance of 1 meter (under the assumed 1 μA current and 6 GeV energy beam, and for a 10 cm LH2 target). For a detector at a distance of 4 m from the target, these radiation doses scale down by a factor of 16. However, these paticle background rates and thus the dose rates are without taking into account the effect of a sweeping magnet. To estimate doses with such a magnet ON as compared to magnet OFF, the dose rates for electrons and positrons were scaled down proportional to the changes in their flux, taken from the simulated distributions with a threshold of 1 MeV.

The realistic background simulations were then cross-checked for an 11 GeV beam energy, with backgrounds found to be very similar (slightly reduced, by ∼10%) as compared to a 6.6 GeV beam energy. This is because the background is predominantly induced by the beam-target interactions, with the envisioned beam pipe only contributing 10-20%. Thus, we have further used the detailed background simulations at 6.6 GeV beam energy, which are well valid for a range of beam energies of ∼6 to 11 GeV.

In Fig. 22 we show the dose rates from photons, electrons, positrons and the total dose versus NPS angle, without sweeper magnet in the top panel, and with 0.3 Tm magnet in the bottom panel (rescaled based on the realistic simulated background fluxes). In Fig. 23 we then show the total dose rates as a function of NPS angle, with magnet on and off, compared to a 50 krad dose limit before UV curing is required, which we feel is a conservative number based on all studies presented (see Fig. 21).

The 50 krad dose limit is conservative as (i) even at much higher integrated doses only small (few %) effects are seen in Fig. 21; (ii) we do not take into account any additional shielding materials; and (iii) actual dose rates out-of-plane are much reduced. In addition, we integrated over all the low-energy particles included in the realistic background simulations, when in reality one would not anticipate much damage from electrons with energies below 1-2 MeV.

At the smallest NPS angle of 5.5^o the dose rate is ∼400-500 rad/hr for the sweeping magnet field OFF and ∼40-50 rad/hr for the field ON configuration, assuming a 1 μA beam current and a 10 cm LH2 target. Thus, one can take these numbers and the conservative 50 krad dose limit and scale to what can be considered acceptable

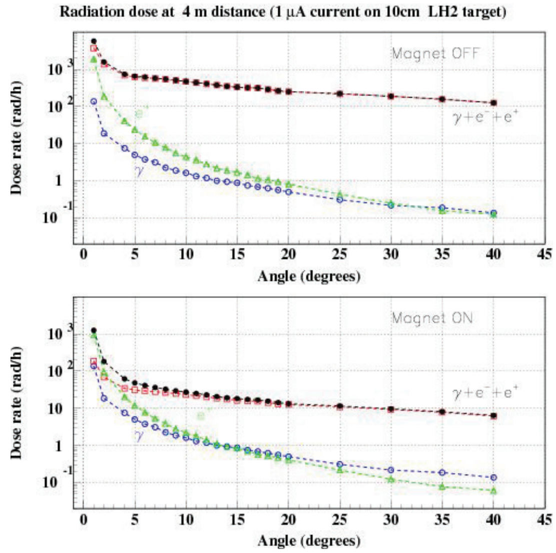

FIG. 22: *NPS detector Radiation dose rates from photons, electrons and positrons, and combined dose rates as a function of angle with sweep magnet OFF (top)and ON (bottom). The detector is at the distance of 4 m from the 10 cm LH2 target. The beam energy and current are 6.6 GeV and 1.0 μA.*

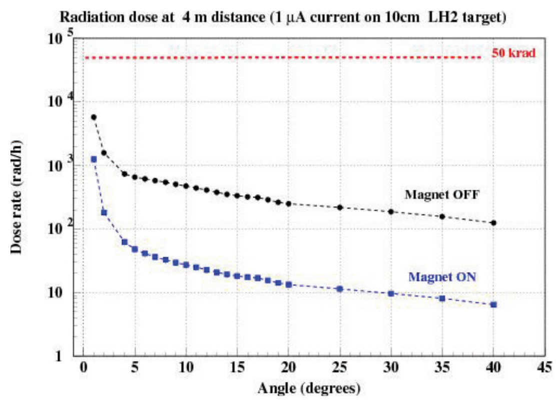

FIG. 23: *NPS detector Combined Radiation dose rates from photons, electrons and positrons as a function of angle, with sweep magnet OFF and ON. The detector is at the distance of 4 m from the 10 cm LH2 target. The beam energy and current are 6.6 GeV and 1.0 μA.*

running (luminosity) conditions. Or, if light output variations of up to a few % are acceptable for the physics of interest, one can relax the conservative 50 krad dose limit somewhat, possibly to a few 100 krad dose limits *.

* The energy spectrum and flux of the background particles were used to calculate the dose rates. For simplicity, we used the energy deposition of the particles in a small front surface layer of the $PbWO_4$ detector to normalize to 1 kg of matter. This is because the realistic background calculations performed by Pavel Degtiarenko of the JLab Radiation Control group uses as units Rem/hours (or Rad/hours) for dose rates, which corresponds to a 1 *J* energy deposition in 1 *kg* of matter. Hence, those dose rates correspond as calculated to those doses accumulated in frontal area of the $PbWO_4$ crystals. The simulations as performed do not provide information about the fall-off of radiation dose distribution along the thickness of the $PbWO_4$ crystals yet, as initial layers of the crystal will act as a shield for the deeper layers. This is another reason why our estimated dose rates are conservative as presented.

[1] Physics Opportunities with the 12 GeV Upgrade at Jefferson Lab, J. Dudek et al., Eur. Phys. J. A48 (2012) 187.

[2] M.E. Christy et al., Phys. Rev. C70 (2004) 015206.

[3] A Precision Measurement of the Neutral Pion Lifetime via the Rrimakov Experiment, JLab Proposal E02-103, A. Gasparian, S. Danagoulian spokespersons.

[4] M. Kubantsev et al., Performance of the Primex Electromagnetic Calorimeter, arXiv:physics/0609201, 22 Sep. 2006; A. Gasparyan, Performance of PWO crystal Detector for a High Resolution Hybrit Electromagnetic Calorimeter at Jefferson Lab., Proceed. X Int. Conf. Calorimetry in Particle Physics, Perugia, Italy, 29 March-2 April 2004, pp. 109-115.

[5] P. Lecoq et al., Nucl. Instr. and Meth. A 365, 291 (1994); A402, 75 (1998); A403, 302 (1998). .

[6] Shi Chao-Shu, Chin. Phys. Lett. **15**, 55 (1998).

[7] G. Franzoni et.al, Nucl. Instrum. Meth. A628, 90 (2011).

[8] R. Niyazov et al., Inner Calorimeter in CLAS/DVCS Experiment, Proc. of the Int. Workshop Exclusive Reactions at High Momentum Transfer, JLab, Newport News, VA, 21-24 May 2007, pp.421-424; V. D. Burkert et all., CEBAF experiment E01-113

[9] Measurement of the Ratio $R = \sigma_L/\sigma_T$ in Exclusive and Semi-Inclusive π° Production, Proposal to Jefferson Lab PAC38/PAC39, T. Horn, R. Ent, H. Mkrtchyan spokespersons.

[10] P. Bosted, R. Ent, and H. Mkrtchyan, Measurement of the Ratio $R=\sigma_L/\sigma_T$ in Semi-Inclusive Deep-Inelastic Scattering, proposal to Jefferson Lab PAC30.

[11] L. Nagornaya et al., IEEE Transactions on Nuclear Science, Vol. 44, No. 3, p.866, June 1997.

[12] R. Y. Zhu et al., IEEE Transactions on Nuclear Science, Vol. 45, No. 3, p.686, June 1998.

[13] Pavel Degtiarenko, private communication.

[14] Bitao Hu, The analysis of primex test run on September 15. PRIMEX analysis documentation.

[15] V. Popov, H. Mkrtchyan, New potomultiplier active base for Hall C Jefferson Lab Lead Tangstate Calorimeter, NSSS2012-1098.

[16] V. A. Batarin et.al, (BTeV electromagnetic calorimeter group), Nucl. Instrum. Meth. A512, 488 (2003), hep-ex/0210011.

[17] A. Fyodorov et al., Rad. Meas. 26, 107 (1996)..

[18] R. Y. Zhu et al. Nucl.Instrum.Meth, A 413, 297 (1998)

[19] P. Adzic et al., The CMS Electromagnetic Calorimeter Group report, http://iopscience.iop.org/1748-0221/5/03/P0310, 2010.

[20] R. Chipaux et al., Proc. Mat. Res. Soc. Symp. 348 (1994) 481

[21] R. Chipaux and O. Toson, Proc. Int. Conf. Intorg. Scint. Appl., 1,(1995) 274

[22] M. Kh. Ashurov et al., Atom. Energy 91 (2001) 560

[23] R. Chipaux et al., Proc. 8th Int. Conf. Inorg. Scint.pg.369-371, Alushta, 2005

[24] H.Huhtinen et al., ETHZ-IPP-PR-2004-03, Swiss Institute for Particle Physics

[25] R. Y. Zhu et al., Nucl. Instr. and Meth. A376, 319 (1996); C. Woody et al., Proc. of SCINT95 Int'l Conf. Delft, August 1995 and IEEE-NUCL-S V43 (1996) 1585.

[26] Qu Xiangdong, A Study of Lead Tungstate Crystals and Improvement of Radiation Hardness. Ph.D. Thesis, Shanghai Institute of Ceramics. The Chinese Academy of Sciences, Shanghai, China, January 16, 2001.

[27] M. Kobayashi et al., Nucl. Instr. and Meth. A 406, 442 (1998); A 404, 149 (1998); A 399, 261 (1997); A 373, 333 (1996)

[28] S. Baccaro et al., Proc. SCINT97, Shanghai (1997) 203.

[29] M. Nicl et al., Phys. Stat. Sol. A164 (1997) R9; J. Appl. Phys. Lett. 82(11), 5758 (1997); J. Appl. Phys. Lett. 71,(26), 3755 (1997).